
# NAVAL POSTGRADUATE SCHOOL

**MONTEREY, CALIFORNIA**

# THESIS

**ANALYSIS OF WAVE-INDUCED FORCING ON A SUBMERGED BODY AT VARIOUS PITCH ANGLES**

by

Bennitt L. Hermsen

June 2020

Thesis Advisor: Young W. Kwon
Co-Advisor: Joseph Klamo

THIS PAGE INTENTIONALLY LEFT BLANK

| REPORT DOCUMENTATION PAGE | *Form Approved OMB No. 0704-0188* |
|---|---|



| **1. AGENCY USE ONLY** *(Leave blank)* | **2. REPORT DATE** June 2020 | **3. REPORT TYPE AND DATES COVERED** Master's thesis |
|---|---|---|

| **4. TITLE AND SUBTITLE** ANALYSIS OF WAVE-INDUCED FORCING ON A SUBMERGED BODY AT VARIOUS PITCH ANGLES | **5. FUNDING NUMBERS** |
|---|---|
| **6. AUTHOR(S)** Bennitt L. Hermsen | |
| **7. PERFORMING ORGANIZATION NAME(S) AND ADDRESS(ES)** Naval Postgraduate School Monterey, CA 93943-5000 | **8. PERFORMING ORGANIZATION REPORT NUMBER** |
| **9. SPONSORING / MONITORING AGENCY NAME(S) AND ADDRESS(ES)** N/A | **10. SPONSORING / MONITORING AGENCY REPORT NUMBER** |

**11. SUPPLEMENTARY NOTES** The views expressed in this thesis are those of the author and do not reflect the official policy or position of the Department of Defense or the U.S. Government.

| **12a. DISTRIBUTION / AVAILABILITY STATEMENT** Approved for public release. Distribution is unlimited. | **12b. DISTRIBUTION CODE** A |
|---|---|

**13. ABSTRACT (maximum 200 words)**

This experiment aimed to quantify the effect of pitch angle on the linear and nonlinear wave-loading of a submerged, cylindrical body. The lower-frequency nonlinear loads that occur in a multi-component seaway were also investigated in greater detail for the zero-pitch case. Unmanned Underwater Vehicles (UUVs) are of increasing interest for use in littoral zones so performance parameters need to be well defined for better design and control. A model was subjected to single and two-component wave trains for pitch angles between -15° and +15° at a depth of 1.5D (model diameter). The results show a negligible difference in vertical force and pitch moment for this range of pitch angles. There was a small increase in drag force at ±15°. The two wave tests validated the use of superposition for predicting linear loads in a multi-component seaway. The smaller low-frequency, nonlinear drag and vertical forces have similar trends with a maximum around a 0.4 Hz frequency difference. The nonlinear pitch moment increases with frequency difference over the range tested. The low-frequency nonlinear loads show a dependence on frequency difference.

| **14. SUBJECT TERMS** submerged body, cylinder, waves, Unmanned Underwater Vehicles, UUVs, pitch angle | **15. NUMBER OF PAGES** 63 |
|---|---|
| | **16. PRICE CODE** |

| **17. SECURITY CLASSIFICATION OF REPORT** | **18. SECURITY CLASSIFICATION OF THIS PAGE** | **19. SECURITY CLASSIFICATION OF ABSTRACT** | **20. LIMITATION OF ABSTRACT** |
|---|---|---|---|
| Unclassified | Unclassified | Unclassified | UU |

NSN 7540-01-280-5500 Standard Form 298 (Rev. 2-89) Prescribed by ANSI Std. 239-18

THIS PAGE INTENTIONALLY LEFT BLANK

**Approved for public release. Distribution is unlimited.**

# ANALYSIS OF WAVE-INDUCED FORCING ON A SUBMERGED BODY AT VARIOUS PITCH ANGLES

Bennitt L. Hermsen
Ensign, United States Navy
BS, U.S. Naval Academy, 2019

Submitted in partial fulfillment of the
requirements for the degree of

**MASTER OF SCIENCE IN MECHANICAL ENGINEERING**

from the

**NAVAL POSTGRADUATE SCHOOL**
**June 2020**

Approved by: Young W. Kwon
Advisor

Joseph Klamo
Co-Advisor

Garth V. Hobson
Chair, Department of Mechanical and Aerospace Engineering

THIS PAGE INTENTIONALLY LEFT BLANK

# ABSTRACT

This experiment aimed to quantify the effect of pitch angle on the linear and nonlinear wave-loading of a submerged, cylindrical body. The lower-frequency nonlinear loads that occur in a multi-component seaway were also investigated in greater detail for the zero-pitch case. Unmanned Underwater Vehicles (UUVs) are of increasing interest for use in littoral zones so performance parameters need to be well defined for better design and control. A model was subjected to single and two-component wave trains for pitch angles between -15° and +15° at a depth of 1.5D (model diameter). The results show a negligible difference in vertical force and pitch moment for this range of pitch angles. There was a small increase in drag force at ±15°. The two wave tests validated the use of superposition for predicting linear loads in a multi-component seaway. The smaller low-frequency, nonlinear drag and vertical forces have similar trends with a maximum around a 0.4 Hz frequency difference. The nonlinear pitch moment increases with frequency difference over the range tested. The low-frequency nonlinear loads show a dependence on frequency difference.

THIS PAGE INTENTIONALLY LEFT BLANK

# Table of Contents

# List of Figures

# List of Tables

THIS PAGE INTENTIONALLY LEFT BLANK

# List of Acronyms and Abbreviations

**NPS** Naval Postgraduate School

**UUVs** Unmanned Underwater Vehicles

THIS PAGE INTENTIONALLY LEFT BLANK

# Acknowledgments

I would like to thank Dr. Kwon and Dr. Klamo for their knowledge and time during this project. I would also like to thank Mr. John Mobley for his expertise in machining parts for this thesis. Thank you to ENS Sabella Goodwin and ENS Zach Klein for assisting in the lab. A final thank you goes to ENS Molly Hannan for her dedicated support—this work would not have gone as smoothly without her efforts.

THIS PAGE INTENTIONALLY LEFT BLANK

# CHAPTER 1:
# Introduction

## 1.1 Motivation

The main goal of this work was to analyze the wave forcing on a submerged, cylindrical body at various pitch angles and frequencies of combined waves. Data from this experiment will supplement existing knowledge for the programming and control of Unmanned Underwater Vehicles (UUVs) near the surface. Testing at more parameters is also helpful for determining potential mission sets and limitations in near surface operations.

As the Navy focuses more of its efforts on the potential uses of unmanned systems, the need for accurate control and reliability is paramount. For the 2020 fiscal year alone, the Navy budgeted $359 million for UUVs and projected a procurement of 191 vehicles between 2019 and 2024 [1]. This investment is a reflection of the importance UUVs have in future operational uses. UUVs have the potential to take on missions deemed too dangerous for humans, to increase endurance, and to expand the Navy's reach in littoral zones. Tasking the dangerous and mundane missions to UUVs will also alleviate the workload on trained Sailors who would then divert their efforts to other critical areas. To achieve this integration into the Fleet, the Unmanned Maritime Systems Program Office has identified five areas of focus: endurance; autonomy and precision navigation; command, control, and communications; payloads and sensors; and platform integration [2]. Accuracy and reliability in navigation and control require a comprehensive understanding of forces acting on a submerged body to assess and respond passively and in real-time. A more robust understanding of wave loading on a submerged body will aid in the appropriate sizing of control surfaces and fine-tuning of model-based predictive control algorithms on UUVs.

Possible military applications of UUVs range from battlespace awareness to mine sweeping to payload delivery [2]. To develop a full sense of mission capabilities, the range of operation needs to be clearly defined. For instance, the capability of carrying advanced payloads and sensors requires a stable platform and the ability to quickly respond to environmental conditions. Even the ability to launch and recover UUVs is dependent on the environmental

conditions and how stable the vehicle is for coordination with the launch platform. The key to expanding the use of UUVs is a more complete understanding of environmental conditions on its controls.

## 1.2 Previous Work

There have been many experimental and theoretical studies completed on free surface flow over submerged, cylindrical bodies. However, literature on the specific case of vehicles moving under waves is less extensive. W.E. Cummins conducted theoretical research to characterize the forcing on a slender, circular body under a regular wave train using potential theory [3]. His conclusion was a set of simplified force and moment equations to produce non-dimensionalized coefficients for any arbitrary body of revolution. More detailed derivation of the equations follow in Chapter 2. Lee and Newman [4] furthered this approach and produced a set of equations for any slender, arbitrary body—not necessarily a body of revolution. Wilmott [5] then derived equations for the nonlinear vertical force that accounted for forward speed. Another theoretical approach was done by R.J. Englert and J.R. Thurne [6] to compare with Cummins' potential theory derivation. Their approach utilized Morrison's superposition theory, which adds inertial and drag components together for the total force on a body, which is dependent on Reynolds number. To compare the accuracy of the two approaches, an experimental study was also performed. The superposition theory predicted results better in cases where viscous forcing was important, but has the disadvantage of more complicated equations.

Numerical work has also been conducted to simulate the load conditions on submerged bodies. Pinkster [7] used three-dimensional potential theory to estimate the nonlinear loads on a submerged, cylindrical body. He completed an experiment to measure the nonlinear mean loads on a restrained cylinder to validate his numeric work. Crook [8] used a source panel method to simulate the nonlinear mean loads on submerged bodies; he examined effects of geometry and submerged conditions on the loading. A two-dimensional, finite-difference method code was developed by Ananthakrishnan and Zhang [9] to solve the Navier-Stokes equations for a body under a regular wave train. Jones et al. [10] simulated waves in a tow tank on ANSYS CFX to model the loads on a submerged body with a square cross-section.

Experimental work on a horizontal cylinder submerged under a wave train was completed by G.M. Khalil [11]. The cylinder's axis was parallel to the incoming wave crests as the focus was on offshore pilings, not on UUVs. The experiment concluded that the negative drifting force on the body was due to breaking waves over the body which create non-linear forces. The effect of these breaking waves diminished as depth increased. A thesis completed in the same laboratory as this present experiment was done by T.M. Turner [12] to test the influence of cross-sections on wave loading. Four different cross-sections were tested; all of the models had a similar cross-sectional area. The results were that there is a dependence on aspect ratio, and that non-circular cross-sections can reduce or enhance the wave loading. The experiment also revealed a depth dependence where the forcing trends were different below one hull diameter under the surface. Recently, K. Suriben conducted a thesis in this same wave tank to measure the effects of forward speed on wave-forcing and to test the accuracy of Cummins' inviscid potential model when viscous drag is assumed to be important [13]. The results showed that viscous effects were present and do alter the forcing predicted from potential theory.

Another experiment was conducted in this same laboratory by A.R. Whitmer [14]. The focus of his work was to determine if linear superposition is valid for the forcing on a UUV-shaped model under the influence of regular waves. He tested various single-component wave fields followed by combinations of two- and three-component wave fields. The results confirmed that superposition of the linear forces and moments was valid up to three regular waves. The cylindrical model had no forward speed and was tested only at one depth and orientation. These results add to the understanding of wave-body interactions which has applications for fine-tuning control systems areas with complex wave forcing.

## 1.3 Objective

The objective of this work was to measure the effect that pitch angle has on the wave-loading on a submerged body. Specifically, the aim was to determine the ability of superposition to predict the linear loads and to quantify the nonlinear loads. Various pitch angles were tested under single wave conditions and then under combined wave loading. Multiple frequency combinations were used for the combined wave loading. All results were compared to the control case of zero pitch angle. Both the linear and nonlinear loads were analyzed to determine the effect of pitch and frequency differences.

THIS PAGE INTENTIONALLY LEFT BLANK

# CHAPTER 2:
# Theory

## 2.1 Cummins Potential Theory

A UUV or other submerged body experiences wave-induced forcing when in a wave field. Cummins, in the 1950s, used potential flow to develop a set of theoretical equations for a slender body of revolution under a regular, sinusoidal wave train [3]. These net force and moment equations were generic and could account for various body geometries, forward speed, and incoming wave heading. For this experiment, only the drag force, vertical force, and pitching moment ($F_x, F_z, M_y$, respectively) were of interest. The equations were simplified by Turner et al. for this specific model shape of a cylinder with hemispherical end caps, no forward speed, and aligned perpendicular to incoming wave crests [15]. The simplified equations are listed in equations 2.1–2.3.

$$F_x = -\frac{\pi}{2}\rho g A_o h\left(\frac{1}{\lambda^*}\right)e^{-2\pi d'} b_0 \cos\left(\omega_e t\right) \tag{2.1}$$

$$F_z = -\pi\rho g A_o h\left(\frac{1}{\lambda^*}\right)\left(1 - \frac{V}{2c}\right)e^{-2\pi d'} b_0 \sin\left(\omega_e t\right) \tag{2.2}$$

$$M_y = \frac{\pi}{2}\rho g A_o L h\left(\frac{1}{\lambda^*}\right)e^{-2\pi d'}\left(\left(1 - \frac{V}{2c}\right)a_1 + \left(\frac{\lambda^* V}{2\pi c}\right)b_0\right)\cos\left(\omega_e t\right) \tag{2.3}$$

In these equations, $\rho$ is fluid density, $g$ is gravitational acceleration, $A_o$ is cross-sectional area of the model, $h$ is wave height, $\lambda^*$ is wavelength, $\lambda$, non-dimensionalized by model length $L$, $d'$ is a non-dimensional depth of $d/\lambda$, $V$ is the model speed, $c$ is the wave speed, $\omega_e$ is the encounter frequency, and $t$ is time. As these tests were all conducted with no forward speed, the $V$ terms were set to 0. The terms $a_1$ and $b_0$ are integral values that are dependent on model geometry. These values were determined by Turner et al. for a cylindrical model with hemispherical end caps [15]. Using these integral values and equations 2.1-2.3, theoretical values for a specific model and wave train can be calculated. However, these equations do

not capture pitch angle of the model. This work will attempt to quantify the load deviation from these expected, zero pitch equations.

The equations for drag force and vertical force are almost identical, except the vertical force is predicted to be a factor of 2 larger with a response phase shift of $\pi/2$. The pitching moment also follows a similar form, but includes an extra term of model length, $L$, and a separate integral expression. The term $e^{-2\pi d'}$ indicates an exponential decay of forcing with submerged depth; the deeper the model, the less force experienced. This relation is of interest as the model will not be at a single depth when pitched.

## 2.2 Linear Superposition

Real operating environments for submerged vehicles consist of many underlying wave components, making it infeasible to test every possible loading condition. An approach tested by Whitmer, Klamo, and Kwon was to use single wave results to predict loads caused by two-component wave trains [16]. They found that this approach was valid for computing the linear loads using regular waves of the same amplitude. However, this method does not capture the nonlinear loading caused by the interactions of multiple waves. These forces arise from the interactions between the waves which result in excitation at the sums and differences of the individual wave frequencies, $f_1 + f_2$, $|f_1 - f_2|$, $2f_1$, $2f_2$, and 0. The 0 combination and the difference combination, $|f_1 - f_2|$, are typically the most important since the other frequency combinations result in the forcing frequency being too high for the body to respond. In the experiment, the nonlinear loads were considerably less in magnitude so did not greatly affect the results. There are situations where the nonlinear effects could be important. For instance, a nonlinear load could excite a natural frequency causing a greater response than expected. To accurately model complex wave loading, superposition can be used for linear loads along with another method for nonlinear loads.

# CHAPTER 3:
# Experimental Set-Up

## 3.1 Laboratory

This experiment took place in the Hydromechanics Laboratory at the Naval Postgraduate School (NPS). The tow tank is 0.914 m (3 ft) wide, 1.219 m (4 ft) deep, and 10.973 m (36 ft) long. It has an aluminum structure with Plexiglass panels for observation of the waves and model during testing. The tow tank and panels are displayed in Figure 3.1. The yellow arrow indicates the direction of wave propagation in the tank. The circle indicates the location of the wave dampening beach. The tow tank is equipped with a towing carriage for forward and backward motion; the carriage was not used in the current experiment as all tests were conducted at zero forward speed.


Figure 3.1. Tow tank and beach used for the experiments.

The waves are produced using a wedge wavemaker that has a 35° interior angle. It oscillates vertically to produce the desired waves; up to a combination of three waves have been used for experimental work in this set-up. The wavemaker is driven by an electric motor

connected to a controller and linear actuator. Details about the motor and controls can be found in the thesis work by Suriben [13]. The wavemaker is in Figure 3.2. The wedge oscillates vertically to create the desired wave environment. A wave dampening beach made of two perforated acrylic sheets is used at the opposite end of the tow tank. The beach is at an incline of approximately 12° to maximize the energy dissipation. The beach is circled in Figure 3.1. The energy dissipation allows for longer experimental runs with less reflected energy in the data.

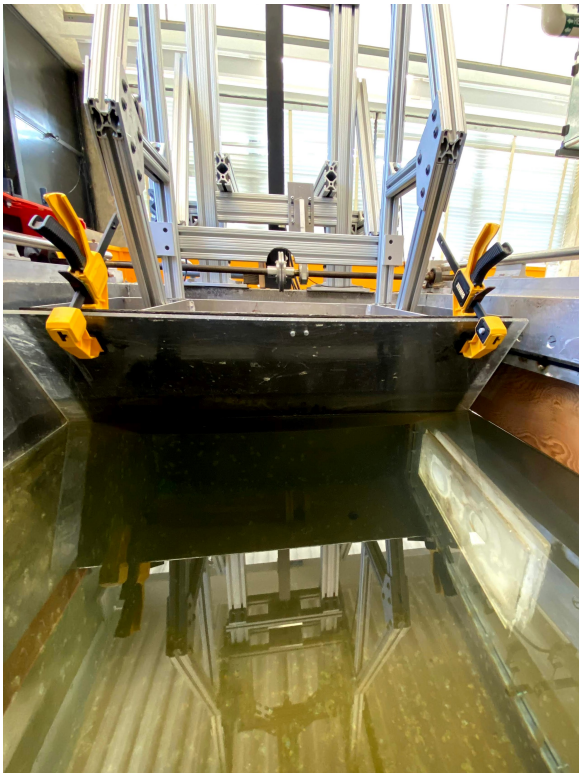

Figure 3.2. The wedge wavemaker oscillated to create the desired wave environment.

## 3.2 Model

The model used was a 15.24 cm (6 in) diameter, aluminum cylinder with a 0.317 cm (1/8 in) wall thickness. A larger cylinder was used than the 11.43 cm (4.5 in) diameter cylinder in previous thesis work in the lab to induce larger nonlinear loads. 3D-printed polycarbonate hemispherical end-caps were attached to the aluminum body. A large clearance hole was

made in the stern end-cap to allow the sting to pass freely without any interference or contact. Bleed holes were made in both the body and the end-caps to ensure a free-flooded model as implemented in Turner's work [12]. The model used is in Figure 3.3. The model was at 0 pitch and 1.5D submerged in this figure

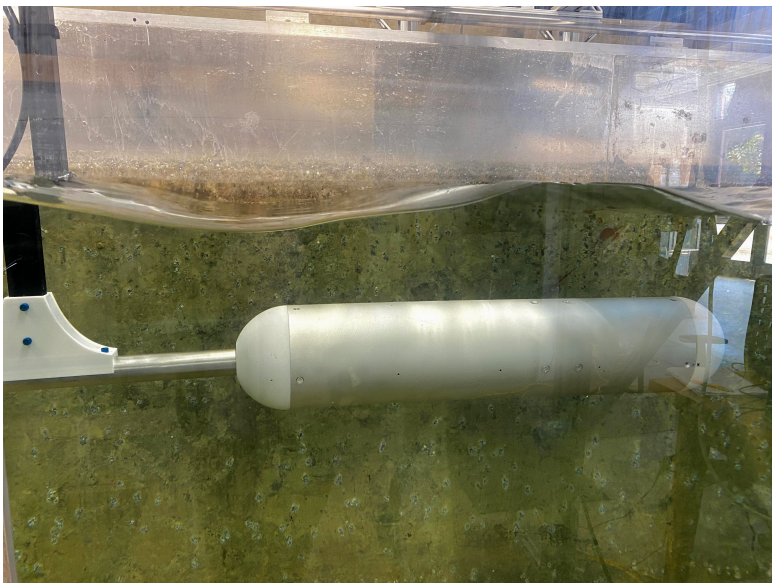

Figure 3.3. Cylindrical aluminum model with hemispherical end-caps used in experiments.

The sting assembly consists of a vertical and horizontal member. The vertical member is a 2.54 cm x 3.81 cm (1 in x 1.5 in) aluminum bar. It is approximately 117 cm (46 in) long with drilled holes in increments of 2.54 cm (1 in) apart. These holes allow for an adjustment in model depth. The vertical sting is affixed to the U-channel in two locations via brackets. The bottom bracket has a series of holes at 3.75° intervals for the change in pitch. The horizontal member is a hollow aluminum rod with a 3.81 cm (1.5 in) outer diameter and a 2.54 cm (1 in) inner diameter. These two members are connected by a custom-made joint. This joint is a polycarbonate printed piece that adapted the existing vertical sting so that previous models can still be used. It connects to the horizontal sting while permitting the cable to pass through unimpeded. The horizontal sting passes through the end cap and affixes to the load cell inside of the model. A photograph of this assembly is included in Figure 3.4.

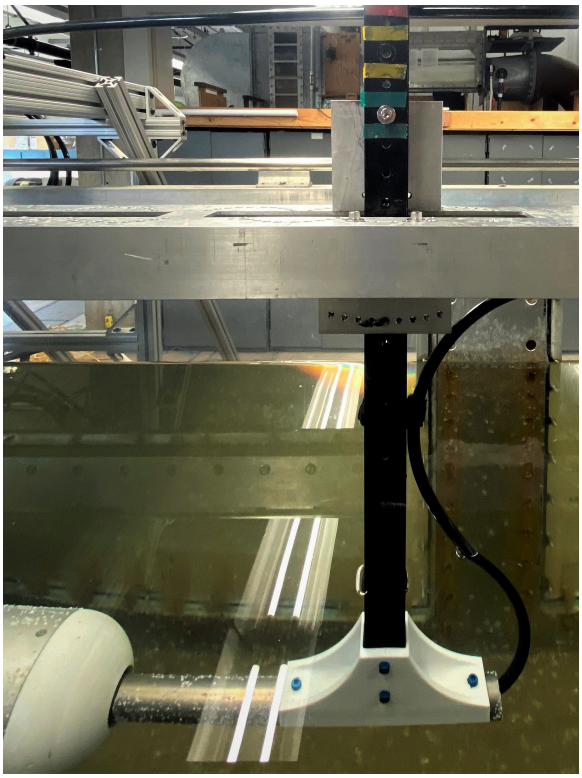

Figure 3.4. Sting and connector used to support the load cell.

## 3.3 Instrumentation

A waterproof load cell was used to measure the wave-induced loads on the model. The load cell is an AMTI UDW3-500, which can measure forces and moments in all three axes. It is stainless steel with a diameter of about 7.6 cm (3 in). The load cell settings and ranges for this experiment are in Table 3.1. The load cell is connected to an AMTI Gen5 amplifier and a signal conditioner to control individual channel settings. A transformation matrix was used during data reduction to convert the load cell axes to the model's coordinate system as defined in Figure 4.1. The load cell axes are denoted with a subscript $L$ and corresponding model axes are denoted with a subscript $M$ in Table 3.1.

Table 3.1. Waterproof Load Cell Parameters.

| Load Cell Axes | $F_{x,L}$ | $F_{y,L}$ | $F_{z,L}$ | $M_{x,L}$ | $M_{y,L}$ | $M_{z,L}$ |
|---|---|---|---|---|---|---|
| Model Axes | $F_{z,M}$ | $F_{y,M}$ | $-F_{x,M}$ | $M_{z,M}$ | $M_{y,M}$ | $-M_{x,M}$ |
| Excitation [V] | 10 | 10 | 10 | 10 | 10 | 10 |
| Gain | 4000 | 4000 | 4000 | 4000 | 500 | 4000 |
| Test Range +/- | 88.9 N (20 lbs) | 88.9 N (20 lbs) | 333.6 N (75 lbs) | 1.69 N-m (15 in-lbs) | 14.12 N-m (125 in-lbs) | 2.26 N-m (20 in-lbs) |

A collar was made to attach the load cell to the horizontal sting and a ring was made to attach the other side of the load cell to the body of the model. This set-up is in Figure 3.5. The left connector attaches to the horizontal sting as shown. The right connector attaches directly to the model. When submerged, the model is only connected to the ring and load cell, not the sting or other support. The load cell is centered in the model. This set-up permits a more direct measurement of forces on the model than in the previous set-up with a non-waterproof load cell. The channels in the ring were made to allow water to easily fill and drain from the model for handling purposes.

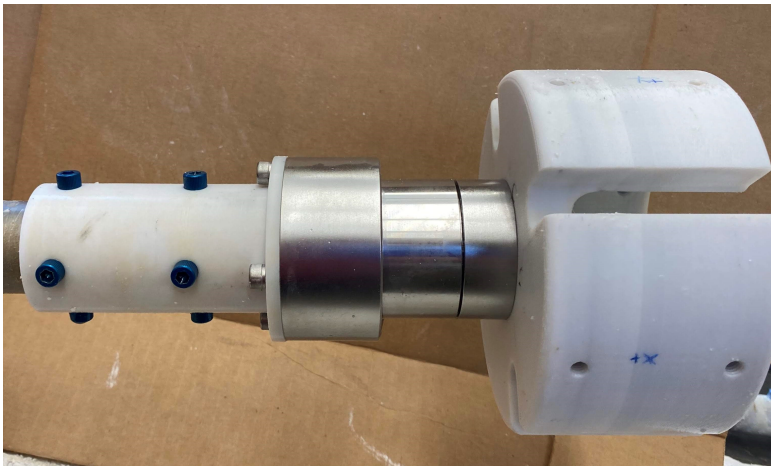

Figure 3.5. The load cell and internal connections used for the experiments.

Previously, the non-waterproof load cell was affixed to the U-channel above the model where the pitching moment had to be moved to the model origin and the forces on the

sting removed. This process introduced more uncertainty in the data. This load cell is an AMTI MC3A with similar load capacities. More details of the non-waterproof load cell and verification of its tolerances are included in the work of Turner [12].

To validate the waterproof load cell and new test set-up, a series of single wave runs were completed using both load cells and the results were compared. The waves ranged from a non-dimensionalized wavelength of 0.750 to 3.250. The wavelength, λ, was non-dimensionalized using the model length, L. The results in Figure 3.6 are for the load cell comparison of the non-dimensionalized axial force, $C_{F\,x}$, and vertical force, $C_{F\,z}$, on the model. These forces are the oscillating linear forces at the wave encounter frequency. 'W' is for the waterproof load cell, and 'N' is for the non-waterproof load cell. Forces are measured in pounds. The horizontal axis is the wavelength, $\lambda$, non-dimensionalized by model length, L.

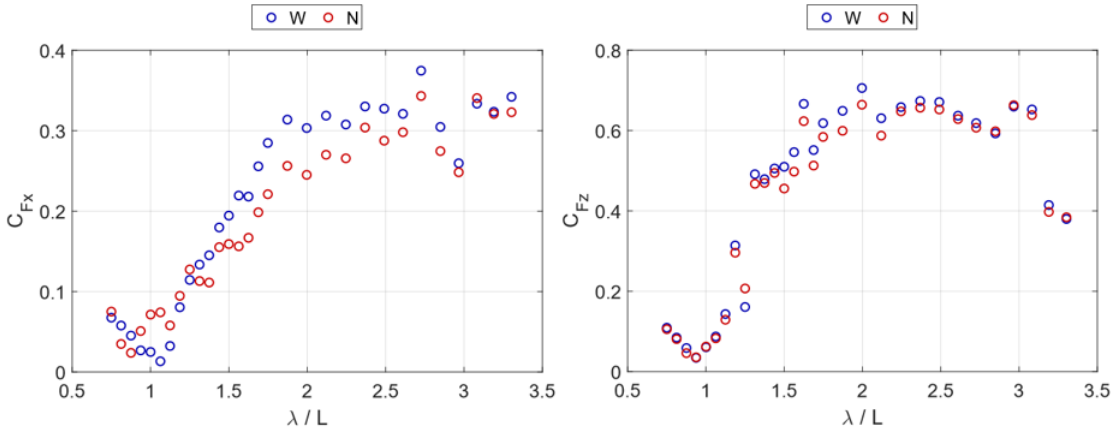


Figure 3.6. Load cell comparison results.

These results validated the waterproof load cell as both measured forces of similar magnitude and followed the same trend. The waterproof load cell is assumed to be more accurate as it is a more direct measurement of forces on the model and does not include uncertainty caused by removing the effects of the sting.

Five Senix ToughSonic 14 ultrasonic probes were used to measure wave height and the displacement of the wedge wavemaker. One probe was positioned above the model to measure any change in the passing wave due to wave-body interactions. Three probes

were located in 15.2 cm (6 in) intervals ahead of the model to measure the incoming wave conditions. The final probe was positioned above the wavemaker to record the wedge oscillations. The load cell and probes were connected to a National Instruments USB-6363 data acquisition board to control the sampling rate of collection and convert the analog voltage inputs to digital outputs. This board was then connected to a laptop to monitor the experimental run. The three probes located ahead of the model are in Figure 3.7.

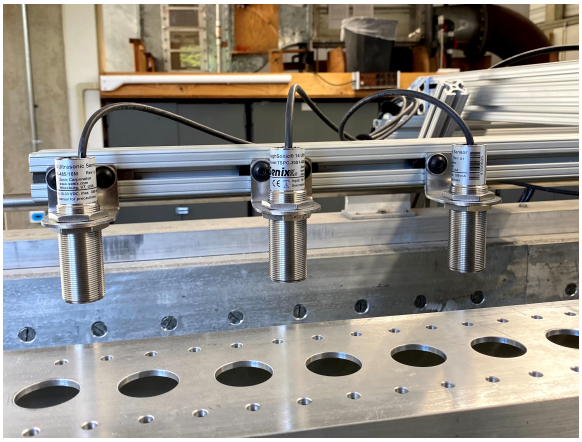

Figure 3.7. Senix wave probes measured wave height ahead of the model.

THIS PAGE INTENTIONALLY LEFT BLANK

# CHAPTER 4:
# Testing

## 4.1 Testing Matrix

The first set of tests were completed to measure the effect that pitch angle has on the nonlinear loads and the ability to use superposition for the linear loads. The model was tested at various angles ranging from -15° to +15° ; the sign convention for the experiment is noted in Figure 4.1. The model is at a pitch of +7.5° in this Figure. Local axes are along the model's axes. Global axes are a fixed reference frame with respect to the tow tank. In the coordinate systems, a negative pitch angle corresponds to the nose of the model closer to the surface, and a positive pitch angle corresponds to the aft end of the model closer to the surface; this is consistent with the convention for a right-handed system with the positive z-axis up. The positive y-axis for both systems is into the page.

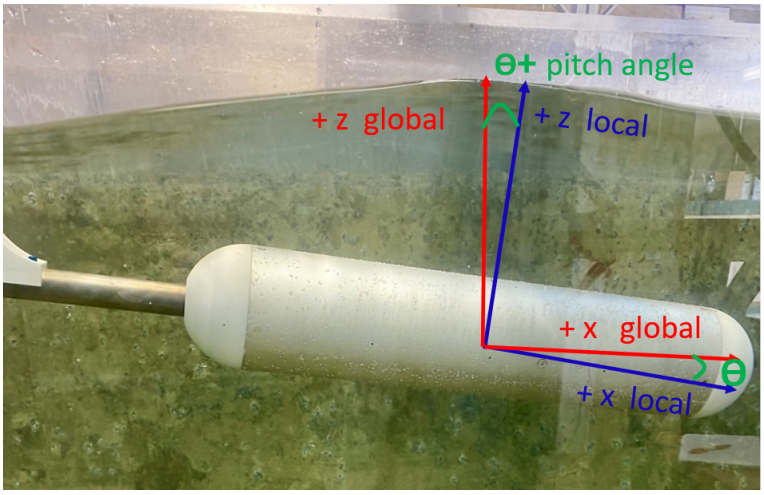


Figure 4.1. The positive sign convention is shown in both the local and global coordinate systems.

At each pitch angle, the model was subjected to single-component and two-component wave trains. The single-component waves all had an approximate 2.54 cm (1 in) amplitude and ranged from $\lambda/L = 0.75$ to 3.00. The two-component waves had these same waves as well as

a 1.27 cm (0.5 in) amplitude wave with a $\lambda$ /L = 2.00, which was held constant. An example testing sequence is included in Appendix A.

The model was submerged to a centerline depth of 1.5 model diameters (1.5D) for the majority of pitch tests. A range of pitch angles from -15° to +15° were tested. It was also submerged to a centerline depth of 2D for a 0° pitch and a -15° pitch to compare depth effects and ensure any surface interactions were not interfering with results at 1.5D. A summary of these tests is included in Table 4.1.

Table 4.1. Pitch Angle Test Parameters.

| Depth/D | Pitch Angle [°] |
|---|---|
| 1.5 | +15 |
| | +7.5 |
| | 0 |
| | -7.5 |
| | -15 |
| 2 | 0 |
| | -15 |

The next set of tests involved a detailed study of the nonlinear loads on the model, specifically the low frequency loads from the presence of multiple waves. The model was kept at 0° pitch and 1.5D. Two-component wave tests were completed using the same range of 2.54 cm (1 in) amplitude waves as used previously. The fixed 1.27 cm (0.5 in) amplitude wave was varied to five distinct non-dimensional wavelengths between $\lambda$ /L = 1 and 3 as summarized with their corresponding frequencies in Table 4.2. An entire sweep of the 2.54 cm (1 in) amplitude waves was completed for each 1.27 cm (0.5 in) amplitude wave.

Table 4.2. Frequency Effect Test Parameters

| λ /L | Frequency [Hz] |
|---|---|
| 1 | 1.716 |
| 1.5 | 1.180 |
| 2 | 1.013 |
| 2.5 | 0.907 |
| 3 | 0.824 |

## 4.2 Testing Procedure

Tests were conducted by first placing the model at the desired pitch and depth. The holes on the vertical sting were used to adjust the model while keeping the water depth in the tank at approximately 96.5 cm (38 in) deep since water depth affects the wave amplitude to wedge amplitude transfer function. The desired wave frequency and peak to peak amplitude were provided to the wavemaker. A run was completed by recording the load and wave time histories for 60 seconds. These were recorded in output voltages to be processed to physical units during analysis. A full pass of the testing sequence was completed for a single wave. A full pass means that each of the wedge frequency and amplitude combinations were tested in a random order. Then, a full pass of the two-component wave runs were completed followed by a half-pass through the testing sequence where every other wave combination was used. In these tests, the 1.27 cm (0.5 in) amplitude wave was kept at a fixed frequency while the 2.54 cm (1 in) amplitude wave was varied in the same manner as the single component runs. This half-pass allowed for more reliability in the data. This process was repeated for each of the tested parameters.

## 4.3 Data Reduction

The data files of raw voltages were used in custom MATLAB scripts to extract the wave parameters and forces. A zero file was taken at the start of each testing sweep to establish electrical offset values for all of the sensors. In the data cleaning process, these values were then removed from the data. Gain values were applied to convert from raw voltages

to physical units. Transformation matrices were used to align the collected data with the established sign conventions for both the local and global coordinate systems as defined in Figure 4.1.

Then, the wave length, $\lambda$, was estimated using the third order, finite-depth dispersion relationship [17] and the wave number relationship in Equations 4.1 and 4.2

$$\omega_i^2 = g k_i \phi_i \left(1 + \frac{9 - 10\phi_i^2 + 9\phi_i^4}{8\phi_i^4}(k_i a_{wi})^2\right) \tag{4.1}$$

$$\lambda_i = \frac{2\pi}{k_i} \tag{4.2}$$

where $\omega_i$ is the wave frequency, which was the same as the wedge frequency, $g$ is the gravitational constant, $k_i$ is the wave number, $\phi_i = \tanh(k_i d)$, $d$ is water depth, and $a_{wi}$ is the wave amplitude. All of these variables are for the $i$th wave component; $i = 1$ for single waves, and $i = 1, 2$ for two-component waves. The wave amplitude used in this calculation is the desired wave amplitude since the achieved amplitude is yet unknown; Klamo et al. found the estimated wavelength using desired amplitude to be within 1.5% of results using achieved wave height [17]. This dispersion relationship was chosen since the waves were steep in some runs and longer than twice the water depth in other runs.

The achieved wave amplitudes and phases were then calculated from the three forward wave probe readings using the least squares curve fit in Equation 4.3.

$$f_1(x,t) = \sum_{i=1}^{n} \left(A_{1,i} \cos(k_i x - \omega_i t) + B_{1,i} \sin(k_i x - \omega_i t)\right) + C \tag{4.3}$$

The sum is for the wave components $i = 1$ to $n$, the total number of wave components. $A_{1,i}$ and $B_{1,i}$ are the amplitudes for the cosine and sine components. These components were combined into a single sine wave of amplitude $a_{wi}$ and phase angle $\phi_{wi}$. $C$ captures the mean of the data set. The spatial dependence accounts for the probe positions so that the phases are all relative to the same location, not the measurement location.

To estimate the drag force, vertical force, and pitching moment on the model, a least squares curve fit was applied to the time history data. The function used is

$$\begin{aligned} f_2(t) = &\sum_{i=1}^{n} \left( A_{1,i} \cos(-\omega_i t) + B_{1,i} \sin(-\omega_i t) \right) \\ &+ \sum_{i=1}^{n} \left( A_{2,i} \cos(-2\omega_i t) + B_{2,i} \sin(-2\omega_i t) \right) \\ &+ A_+ \cos(-|\omega_1 + \omega_2| t) + B_+ \sin(-|\omega_1 + \omega_2| t) \\ &+ A_- \cos(-|\omega_1 - \omega_2| t) + B_- \sin(-|\omega_1 - \omega_2| t) \\ &+ C \end{aligned} \tag{4.4}$$

where, again, $i = 1$ to $n = 2$, the total number of wave components; $A_{1,i}$ and $B_{1,i}$ are the amplitudes of the linear components; $A_{2,i}$ and $B_{2,i}$ are the cosine and sine amplitudes of the nonlinear double frequency term; and $A_+$, $B_+$, $A_-$, and $B_-$ are the cosine and sine amplitudes of the nonlinear components due to multiple frequencies. $C$ is again the mean value of the signal. There is only a time dependence in this function since the load cell readings were taken at the x-origin.

The linear force and moment amplitudes were then calculated by combining the linear cosine and sine portions of Equation 4.4 into a single sine function for each desired quantity $F_x$, $F_z$, and $M_y$ with amplitudes $a_F x$, $a_F z$, and $a_M y$ respectively. The nonlinear, low frequency force and moment components were calculated in a similar fashion from the $A_-$ and $B_-$ terms. The frequency sum and difference terms were not used in the single wave case as its frequency sum and difference is included in the $2\omega$ and the offset terms.

The linear forces and moment were non-dimensionalized using the form by Turner et al. in Equations 4.5 and 4.6 [15].

$$C_F = \frac{a_F}{\rho g A_o h} \tag{4.5}$$

$$C_M = \frac{a_M}{\rho g A_o h L} \tag{4.6}$$

These equations are derived from the coefficients of Equations 2.1-2.3. Desired wave height, $h$, is used to reduce the uncertainty from the wave probe measurements.

The nonlinear terms were non-dimensionalized using Equations 4.7 and 4.8.

$$C_{F,non} = \frac{a_F}{\rho g D h_1 h_2} \tag{4.7}$$

$$C_{M,non} = \frac{a_M}{\rho g D h_1 h_2 L} \tag{4.8}$$

This form allows both wave heights of the nonlinear forcing to be included. The desired wave heights were used, which are twice the component amplitudes. In this experiment, $h_2$ is twice the magnitude of $h_1$. The cross-sectional area becomes the model diameter, D, for proper length scale non-dimensionalization.

# CHAPTER 5:
# Results

## 5.1 Pitch Tests

### 5.1.1 Depth Effects

As mentioned in Section 4.1, tests were completed at 1.5D and 2D for the 0° and -15° pitch angles to ensure surface-body interactions were not influencing results at the submerged depth of 1.5D. The results for the single component axial load, $F_x$, and pitching moment, $M_y$ are included in Figure 5.1. The stars are the results at a submerged depth of 1.5D. The squares are the results at a submerged depth of 2D. Red is the 0° case and blue is the -15° case. The nonlinear vertical loads, $F_z$, from the two-component tests are shown in Figure 5.2. These figures were chosen to provide a breadth of data. They have all been non-dimensionalized as described in Section 4.3.

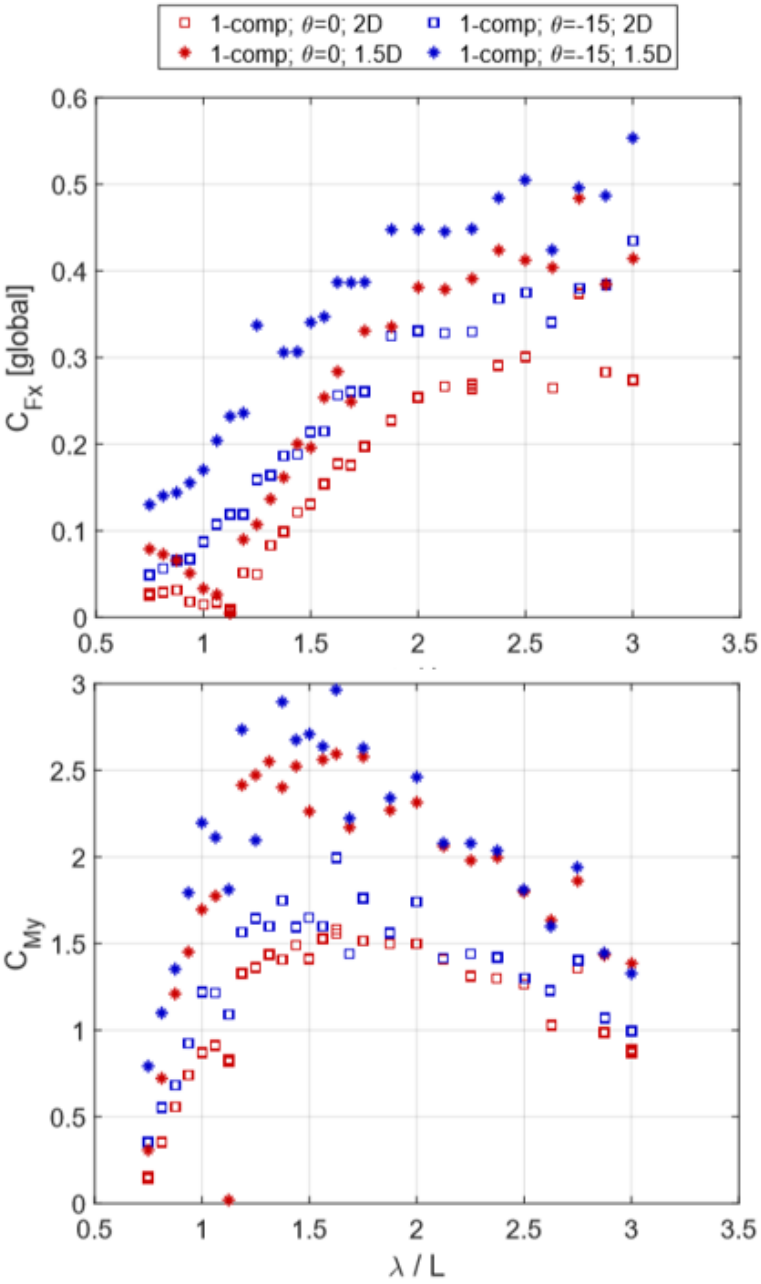


Figure 5.1. These are results of the linear axial load in the global reference frame and the linear pitch moment for the single wave component runs.

These results show a consistent trend in data for model submergence depths of 1.5D and 2D. For the axial load, there is no load at $\lambda/L = 1.1$ for 0° pitch and then continue to increase.

For the pitching moment, there is a steep increase until a maximum occurs near $\lambda/L = 1.5$, then the pitching moment declines. This consistency shows that the surface-body effects were not greatly influencing the data at 1.5D. The loads were larger at 1.5D since there is a depth dependence in wave-loading as seen in Equations 2.1-2.3. Similar consistency was apparent in the low-frequency, nonlinear loads as shown in Figure 5.2. The load is plotted against frequency difference between the wave components. The stars are the results at 1.5D. The circles are the results at 2D. Red is the 0° case and blue is the -15° case.

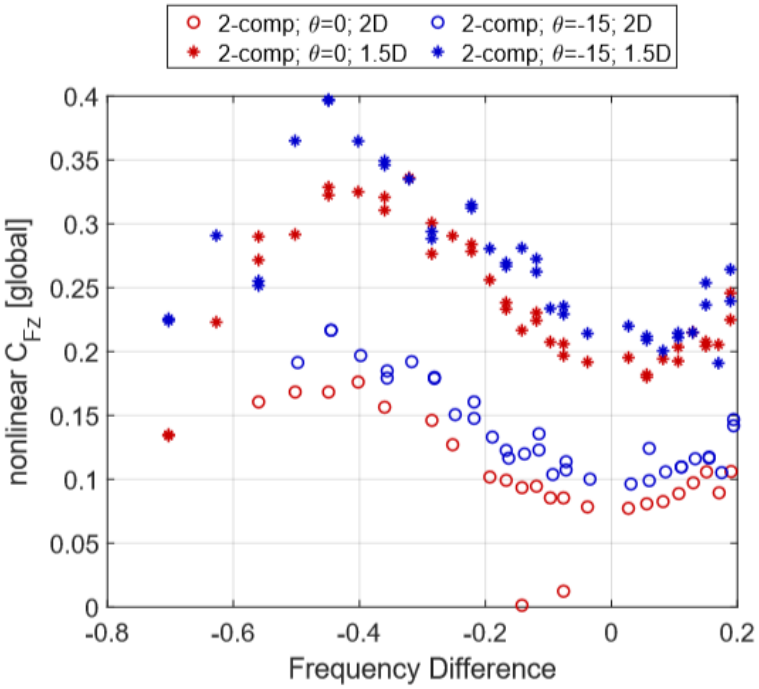


Figure 5.2. These are the non-dimensionalized results from two-component wave runs for the low-frequency nonlinear vertical load in the global reference frame.

For the two-wave tests where the wave amplitude reached 3.81 cm (1.5 in), there were still consistent results between 1.5D and 2D. 1.5D was chosen as the test depth for the remainder of the experiment as the forces were larger. Larger magnitudes were easier to capture, especially in the nonlinear loads where the forces were less than 4.45 N (1 lb).

### 5.1.2 Linear Superposition

The validity of linear superposition to use regular wave results to predict the linear loads of multi-wave runs was confirmed by Whitmer at 0° pitch [14]. This experiment expanded upon those results by testing linear superposition with the addition of varying pitch angle. The linear components for axial force in the global coordinate system is in Figure 5.3. The square markers represent the linear force amplitude results from the single-component wave tests. The circles are the linear load amplitudes corresponding to the 2.54 cm (1 in) amplitude wave from the two-component wave tests. The different colors represent different pitch angles.

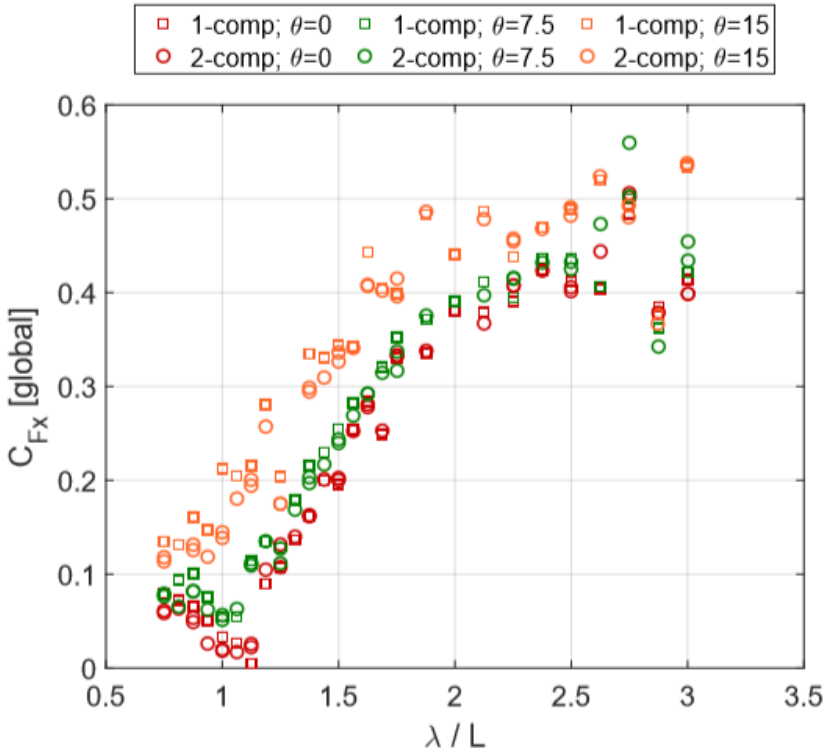


Figure 5.3. The non-dimensionalized axial force is shown with non-dimensionalized wavelength for linear superposition analysis.

Linear superposition was validated as the results from two-component test and single wave tests overlap. This result was consistent for all pitch angles tested. The positive pitch angles are shown for clarity. The negative pitch angles had the same behavior. Only the axial force

is included here for brevity; linear vertical force, $F_z$, and linear pitching moment, $M_y$, for the positive pitch angels are included in Appendix B.

### 5.1.3 Pitch Effects

The effect of pitch angle on loading was then analyzed. Figure 5.4 are the results for the linear axial loads at all pitch angels tested. The results shown are only from the two-component tests for clarity; the regular wave tests had the same results as discussed with linear superposition. The different colors represent different pitch angles.

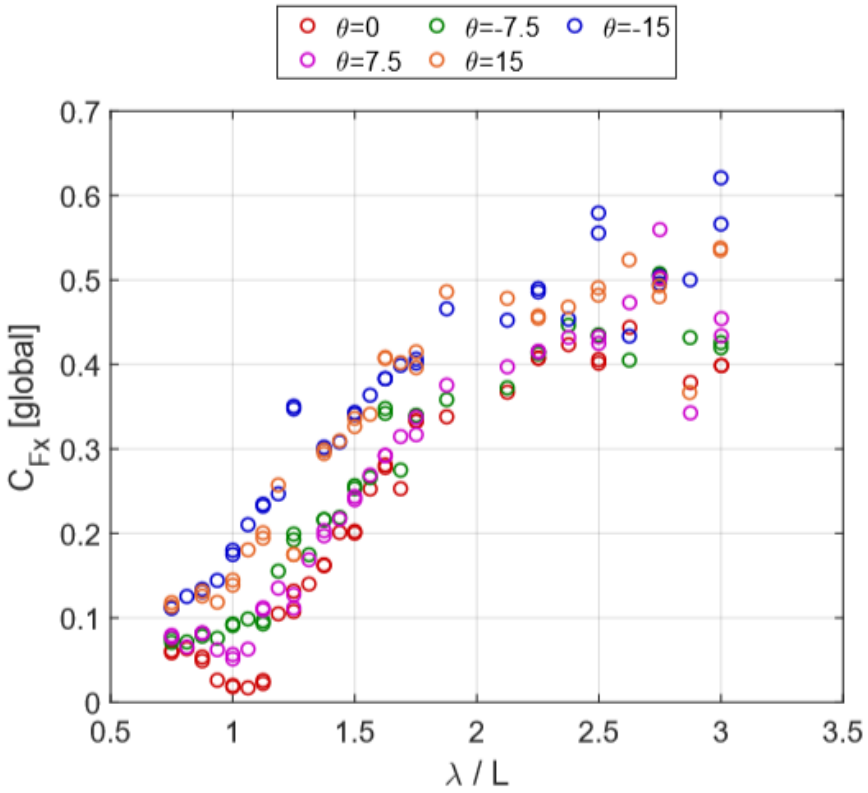


Figure 5.4. The non-dimensionalized axial force is shown with non-dimensionalized wavelength for pitch effect analysis.

The linear axial load at +/-15° is slightly larger than at the control of 0 pitch. Whereas at +/-7.5° , there is not a clear bias. The increase in drag force is not linear with pitch angle.This increase may be attributed to the increase in projected area with respective to the incoming

waves. At 15°, the projected area is approximately 2.3 times as large as the 0°case whereas at 7.5°, the projected area is approximately 1.65 times as large. Also, at 15°, part of the model is closer to the surface where particle velocity is larger in magnitude, which may increase the drag force. The linear axial force is symmetric about pitch angle; the direction of pitch does not affect the load experienced. The local coordinate system results for linear axial and vertical loads are included in Appendix C. The results are similar although the increase at +/-15°is smaller.

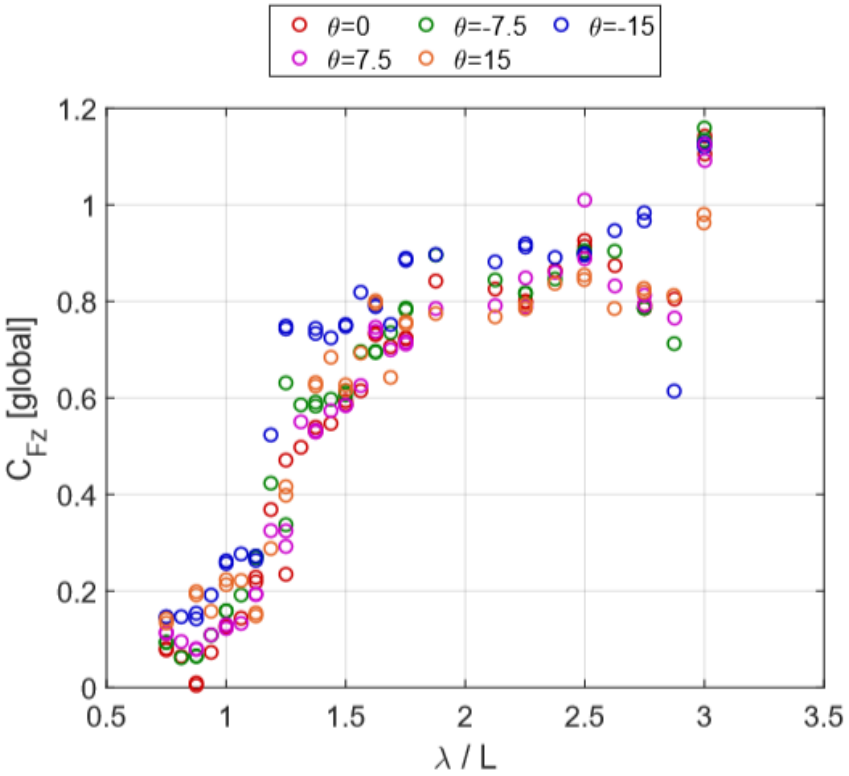


Figure 5.5. The non-dimensionalized vertical force is shown with non-dimensionalized wavelength for pitch effect analysis.

The next load analyzed was the linear vertical load from the global coordinate system in Figure 5.5. The different colors represent different pitch angles. Unlike the axial load, the vertical load does not have the same trend at +/-15° for the entire range tested. The change in planform area is small, which is reflected in the consistency of the vertical force. Between $\lambda/L = 1.25$ and 2.00, there is a slight increase in force for -15° pitch. During testing at

$\lambda/L$ = 1.25 there was an increase in horizontal movement of the model and resonance in the tank. There was a small range of frequencies near this point where a resonant frequency in the tank was excited, affecting the waves or the wave dissipation. The increase in vertical force near this range may be caused by the excess motion of the set-up and not the pitch angle alone. The rest of the results are more clustered and approximately twice the magnitude as the axial forces which was expected.

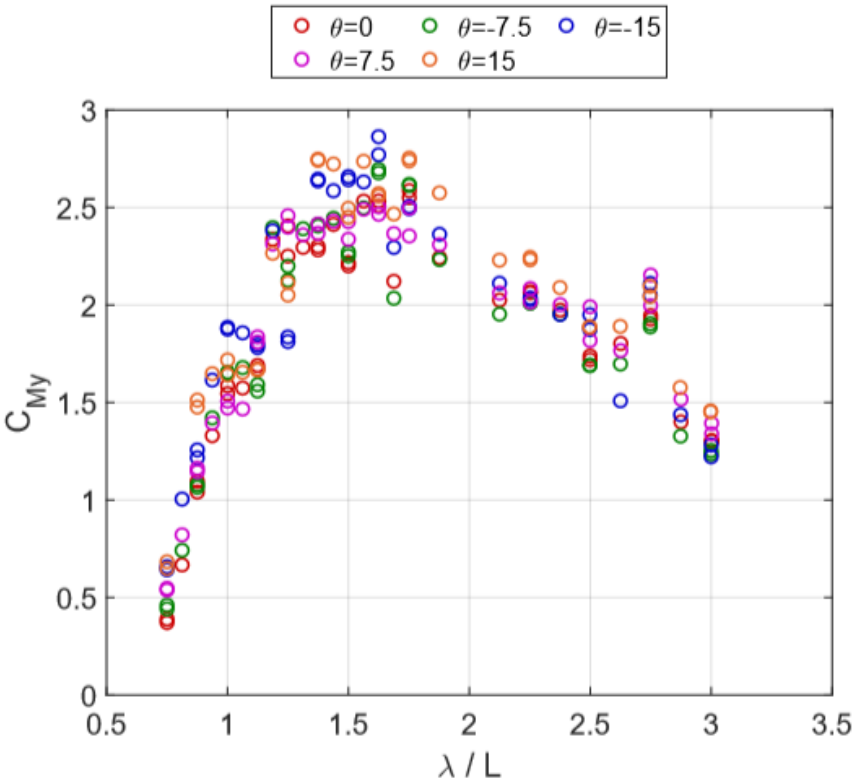


Figure 5.6. The non-dimensionalized pitching moment is shown for pitch effect analysis.

The pitching moment displays similar behavior; its results are in Figure 5.6. The different colors represent different pitch angles. The pitching moment results are clustered throughout most of the range tested. For $\lambda/L$ between 1.25 and 1.75, the pitching moment for the +/-15° cases is slightly larger. This region is where the resonance in the tank occurred. The effect of pitch angle is greatest on the axial component of linear forces analyzed. For the vertical force and pitching moment, the effect of pitch angle is small. The local coordinate system

results for axial and vertical force are similar. They are included in Appendix C.

The pitch angle did have an effect on the mean pitching moment experienced by the model. The mean forces are a result of the zero frequency combination discussed in Section 2.2.

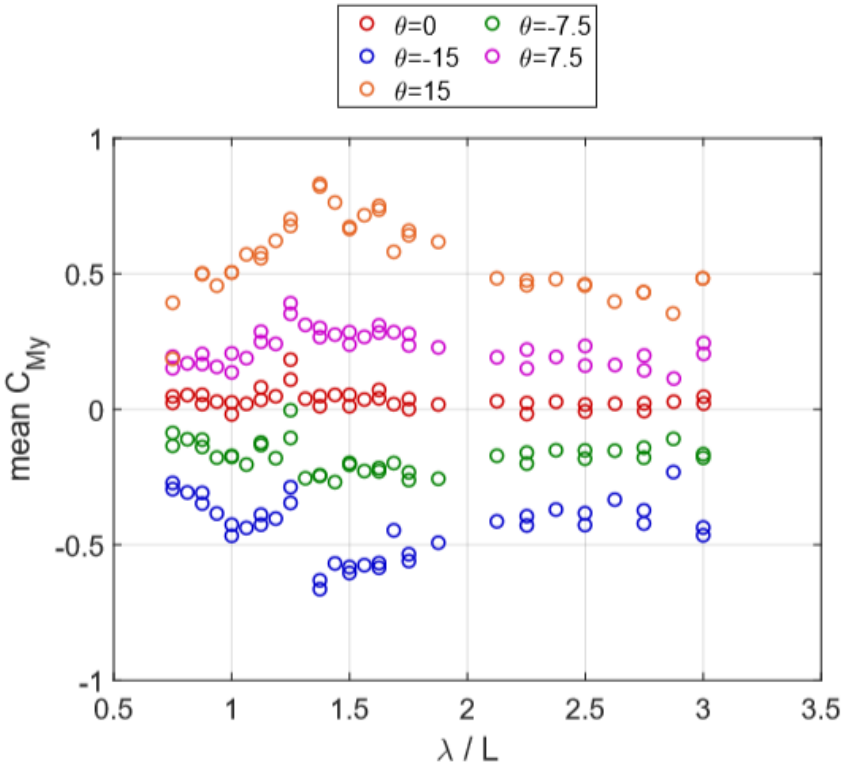


Figure 5.7. The non-dimensionalized mean pitching moment is shown for pitch effect analysis.

The mean load is approximately zero when the pitch angle is at zero as seen in Figure 5.7. This load increases in magnitude with an increase in pitch angle and is symmetric about zero. When at a positive pitch angle, the mean pitching moment is also positive, trying to rotate the model further. The same is true for negative pitch angles. For +/-7.5° , the mean pitching moment remains fairly constant over the range tested. At the pitch angles of +/-15°, there are peaks around $\lambda/L = 1.25$ where the extra horizontal movement occurred. These peaks are caused by resonance in the test set-up.

The effect of pitch angle on low-frequency, nonlinear loads was then analyzed. These

nonlinear loads result from the frequency difference between the two wave components. The nonlinear axial and vertical force components are in Figure 5.8.

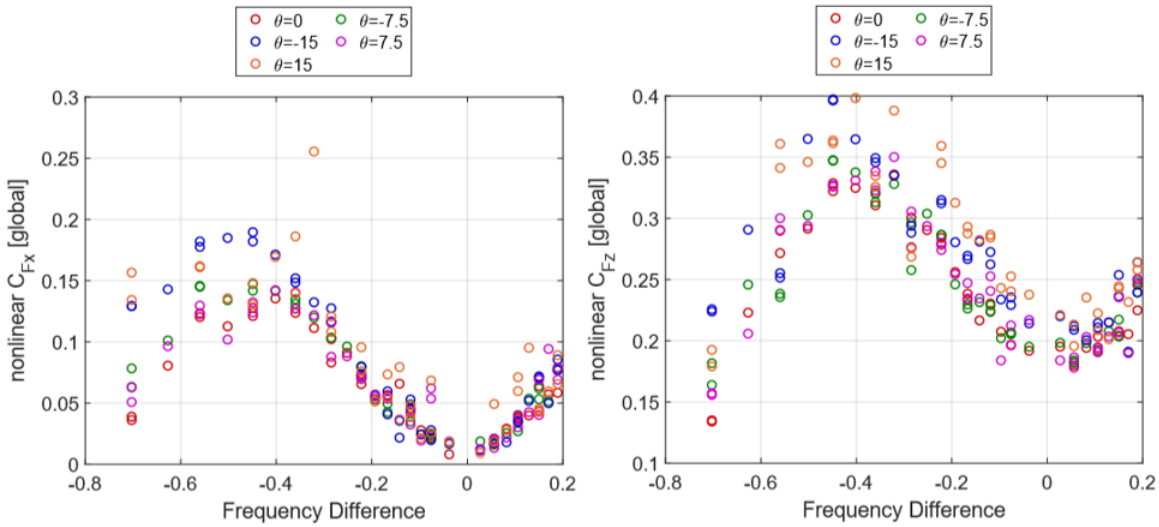


Figure 5.8. The low frequency nonlinear axial and vertical forces are shown with the frequency difference between the wave components.

Both forces have a similar trend with a maximum occurring near a frequency difference -0.4 Hz and a local minimum at 0 Hz difference. The vertical force is larger than the axial force, which is the same trend as the linear forces. Near the maximum value in $F_x$, there is some increase in the +/-15°values. There appears to be minimal effects from pitch angle in $F_x$ over the rest of the tested range. In $F_z$, there exists a small increase in load for +/-15° although the results are still closely clustered. The pitch angle does not have a large influence on the axial and vertical nonlinear forces, but it does on the pitching moment.

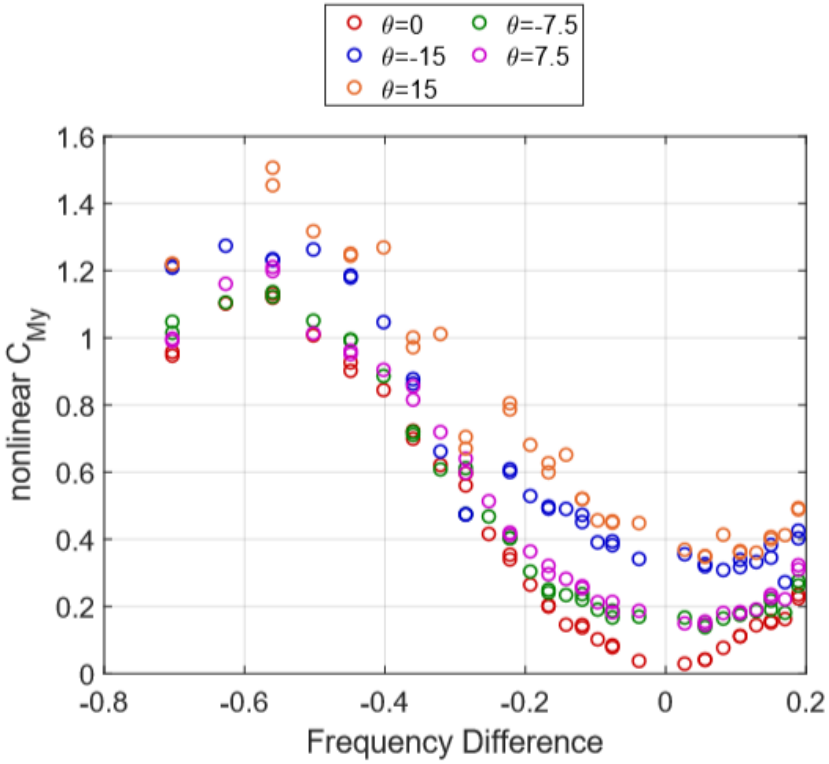


Figure 5.9. The non-dimensionalized nonlinear pitching moment is shown with the frequency difference between the wave components.

The nonlinear pitching moment is affected by the pitch angle. For +/-15° , the pitching moment is larger throughout the tested range of frequency differences. For +/- 7.5° , there is an increase in load between the frequency difference of -0.2 Hz to 0.2 Hz. The overall trend for the nonlinear moment is the same in all pitch angles with a maximum occurring near -0.6 Hz and a local minimum at 0 Hz difference. This trend is consistent with the nonlinear forces in Figure 5.8.

## 5.2 Frequency Tests

The next set of tests were completed for a detailed look at the low-frequency, nonlinear forces. All of these frequency tests had two-wave components and were conducted at zero pitch angle. The fixed wave was varied between $\lambda/L = 1$ and 3. The nonlinear axial and vertical forces plotted versus frequency difference are included in Figures 5.10 and 5.11.

The colors represent the different $\lambda/L$ values that were held constant.

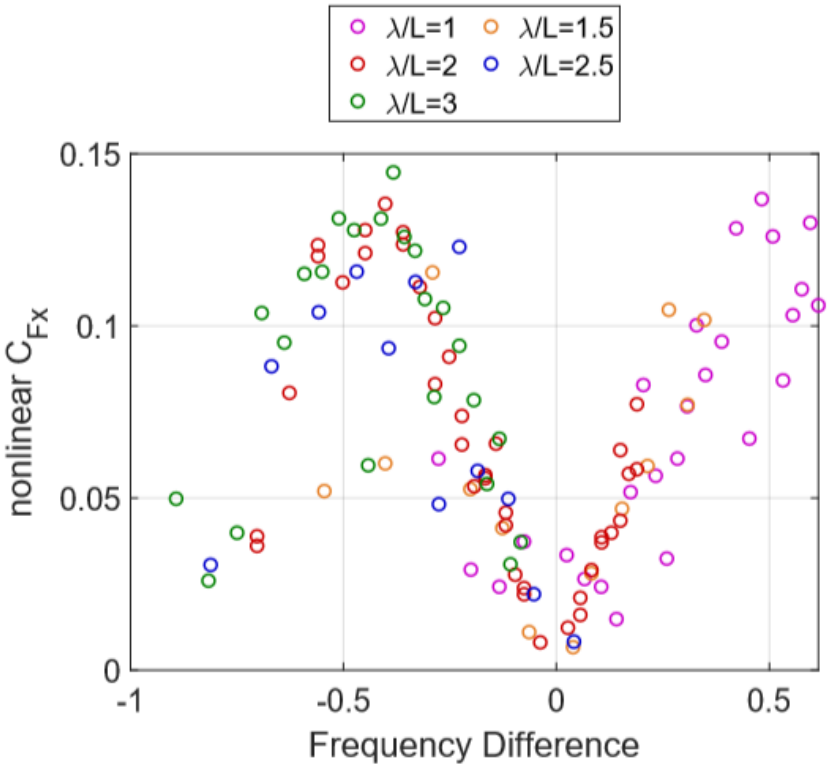


Figure 5.10. The nonlinear axial load is plotted versus the frequency difference of the two wave components.

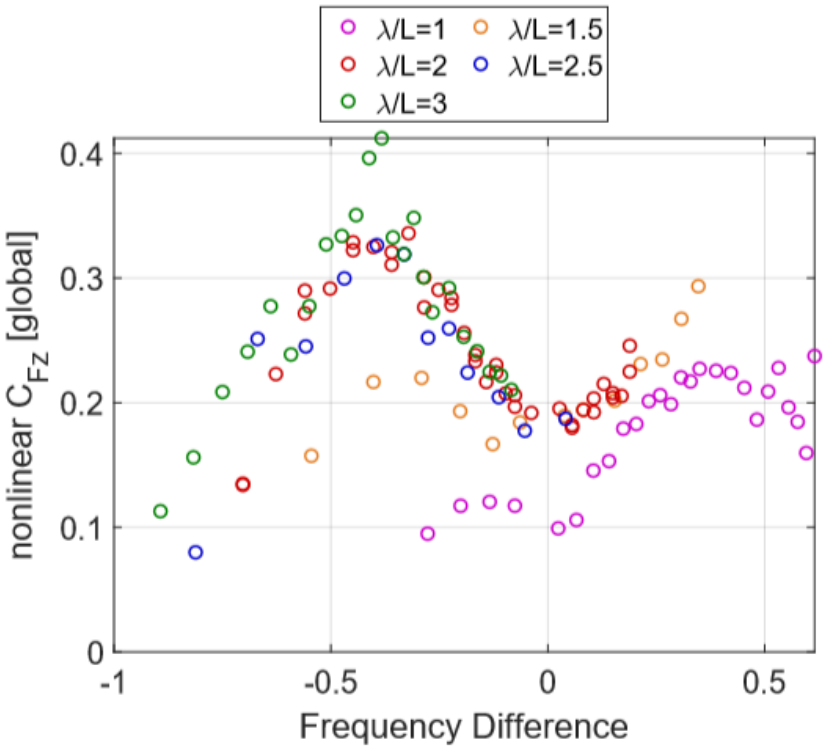


Figure 5.11. The nonlinear vertical load is plotted versus the frequency difference of the two wave components.

Both the axial and vertical nonlinear force components show similar behavior on either side of zero. They both reach maximums at +/- 0.4 Hz frequency difference between the two wave components. This trend is consistent with results in Figure 5.8. In $F_z$, the magenta circles representing the fixed wavelength of $\lambda/L = 1$ are the smallest in magnitude followed by the orange circles of $\lambda/L = 1.5$. The rest of the markers are similar in magnitude. This trend is reasonable since, for a fixed depth, the influence due to the wave increases as the wavelength increases. The magnitude of nonlinear forces is dependent on the frequency difference of combined waves. This relationship is also clear in the pitching moment in Figure 5.12.

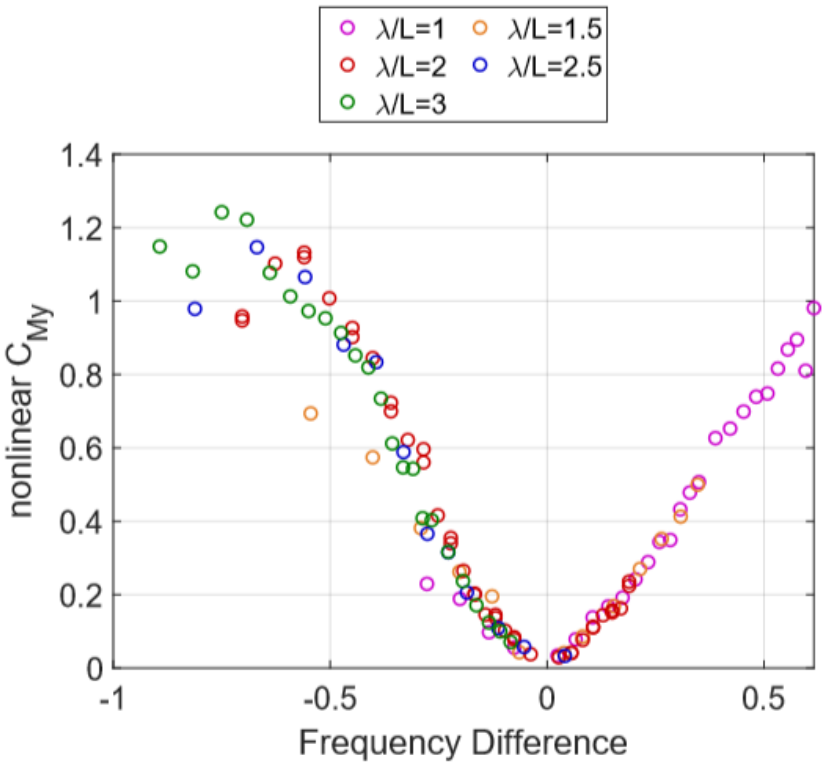


Figure 5.12. The nonlinear pitching moment is plotted versus the frequency difference of the two wave components.

The pitching moment increases as the frequency difference increases in magnitude. The moment continues to increase over the range tested on the positive side of the plot (where the fixed frequency was higher than the changing frequency). On the negative side of the plot, the moment increase until -0.6 or -0.7 Hz at which the data reaches a local maximum and begins to decline. This trend is consistent with Figure 5.9 where the data reaches a maximum near -0.6 Hz frequency difference and then declines. The range of testing stops before the decline of nonlinear moment develops. The effect of frequency difference on the pitching moment is symmetric. The $\lambda/L$ of the fixed wave component alters the magnitude, but not the shape, of the results.

THIS PAGE INTENTIONALLY LEFT BLANK

# CHAPTER 6:
# Conclusions and Future Work

## 6.1 Conclusions

Experiments were completed to analyze the wave-loading of a body at various pitch angles and wave conditions. Single-component and two-component waves were used to examine the linear and nonlinear loads. A detailed study on the nonlinear loads was then completed by varying the frequency difference during two-component testing.

Results from the single and two-component wave tests validated the use of linear superposition with a body at a pitch angle between -15° to +15°; regular wave results can be used to predict the linear loads of complex wave environments. No modification to linear superposition is needed when the body is pitched within the range tested during this experiment. The low frequency, nonlinear loads must be determined using a different method than regular wave testing.

The effect of pitch angle on linear loading was found to be small. An increase in linear drag force occurs at +/-15° as the projected area increases. This force increase is not apparent at +/-7.5°. For the linear vertical force and linear pitching moment, there was no apparent effect from pitch angle. For the axial and vertical nonlinear loads, there was not much effect from pitch. Both nonlinear forces had the same trend with a peak occurring near -0.4 Hz frequency difference between the wave components. Near the peak, there was a slight increase in force for +/-15°, but this trend was not consistent over the tested range. The mean pitching moment, resulting from the 0 frequency combination, increases in magnitude with pitch angle and is symmetric about the zero axis. The nonlinear pitching moment also showed a dependency on pitch angle. The pitching moment was consistently larger for +/-15° and was larger for +/-7.5°over the range of -0.2 Hz to 0.2 Hz frequency difference. Overall, the pitch angle did not have a large effect on the wave-loading on the model. There were small increases in linear axial force, mean pitching moment, and nonlinear pitching moment.

The nonlinear loads exhibited a dependence on the frequency difference between the two

wave components. The axial and vertical nonlinear loads had similar behavior about zero and had the same shape with maximums at +/-0.4 Hz of frequency difference. As the wavelength of the fixed wave component increased, so did the magnitude of the nonlinear force. The nonlinear pitching moment increased as frequency difference increased over the range tested. The nonlinear loads are dependent on the frequency difference of the wave components, not on the actual frequencies of the two waves. These results were consistent with the low-frequency nonlinear loads analyzed for pitch effect.

## 6.2 Future Work

### 6.2.1 Nonlinear Loading Conditions

More testing to understand nonlinear loads is needed to develop an accurate model of complex wave environments interacting with a body. Continued testing with more fixed wavelength combinations and a larger amplitude fixed wave will contribute to a better understanding. Whitmer conducted a three-component wave test to analyze the linear loads [14]. Repeating this test to analyze the nonlinear loads and then expanding on the multi-component test will develop a more robust knowledge of complex seaways. Detailed analysis should also be conducted on the mean loads that result from the zero frequency combination of waves.

### 6.2.2 Test Environment

In order to reduce the horizontal movement and resonance that was creating artificial peaks in the data, the test set-up will need added support in the lateral direction. Also, to achieve larger wave amplitudes and more wave components, the wavemaker vibration needs to be dampened so that the linear actuator does not fault. These improvements will expand the testing ability of the facility.

# APPENDIX A:
# Testing Matrix Example

-7.5 pitch; single wave; 1.5D

| | | |
|---|---|---|
| water depth = | 3.16666667 | (ft) |
| max wave lenth = | 6.33333333 | (ft) |
| Desired Wave Height = | 2 | (inches) |
| model length = | 30 | (inches) |

a_wave / a_wedge = Af^2+Bf+C

| | |
|---|---|
| A = | -0.225376 |
| B = | 1.562162 |
| C = | -0.525838 |

| | desired lambda / L (---) | required wave length (ft) | steepness (---) | k (1/ft) | sigma (---) | omega (rad/s) | freq (Hz) | wedge actua (in) | wedge CMD (mm) | ITERATED wedge CMD (mm) | Run # |
|---|---|---|---|---|---|---|---|---|---|---|---|
| 1 | 0.7500 | 1.875 | 11.25 | 3.351 | 1.00000 | 10.781 | 1.716 | 0.671 | 34.071 | 33.500 | 346 |
| 2 | 0.8125 | 2.031 | 12.1875 | 3.093 | 1.00000 | 10.302 | 1.640 | 0.699 | 35.533 | 37.670 | 366 |
| 3 | 0.8750 | 2.188 | 13.125 | 2.872 | 1.00000 | 9.885 | 1.573 | 0.728 | 36.973 | 38.756 | 354 |
| 4 | 0.9375 | 2.344 | 14.0625 | 2.681 | 1.00000 | 9.516 | 1.515 | 0.756 | 38.393 | 39.830 | 357 |
| 5 | 1.0000 | 2.500 | 15 | 2.513 | 1.00000 | 9.187 | 1.462 | 0.783 | 39.796 | 40.893 | 361 |
| 6 | 1.0625 | 2.656 | 15.9375 | 2.365 | 1.00000 | 8.892 | 1.415 | 0.811 | 41.183 | 41.947 | 348 |
| 7 | 1.1250 | 2.813 | 16.875 | 2.234 | 1.00000 | 8.624 | 1.373 | 0.838 | 42.557 | 42.991 | 368 |
| 8 | 1.1875 | 2.969 | 17.8125 | 2.116 | 1.00000 | 8.379 | 1.334 | 0.865 | 43.920 | 44.028 | 359 |
| 9 | 1.2500 | 3.125 | 18.75 | 2.011 | 0.99999 | 8.155 | 1.298 | 0.891 | 45.274 | 45.057 | 350 |
| 10 | 1.3125 | 3.281 | 19.6875 | 1.915 | 0.99999 | 7.948 | 1.265 | 0.918 | 46.619 | 46.081 | 370 |
| 11 | 1.3750 | 3.438 | 20.625 | 1.828 | 0.99998 | 7.757 | 1.235 | 0.944 | 47.958 | 47.098 | 356 |
| 12 | 1.4375 | 3.594 | 21.5625 | 1.748 | 0.99997 | 7.579 | 1.206 | 0.970 | 49.291 | 48.111 | 352 |
| 13 | 1.5000 | 3.750 | 22.5 | 1.676 | 0.99995 | 7.413 | 1.180 | 0.996 | 50.620 | 49.119 | 363 |
| 14 | 1.5625 | 3.906 | 23.4375 | 1.608 | 0.99992 | 7.258 | 1.155 | 1.023 | 51.946 | 50.124 | 358 |
| 15 | 1.6250 | 4.063 | 24.375 | 1.547 | 0.99989 | 7.112 | 1.132 | 1.049 | 53.269 | 51.125 | 344 |
| 16 | 1.6875 | 4.219 | 25.3125 | 1.489 | 0.99984 | 6.975 | 1.110 | 1.075 | 54.590 | 52.123 | 360 |
| 17 | 1.7500 | 4.375 | 26.25 | 1.436 | 0.99978 | 6.845 | 1.089 | 1.101 | 55.911 | 53.119 | 355 |
| 18 | 1.8750 | 4.688 | 28.125 | 1.340 | 0.99959 | 6.607 | 1.051 | 1.153 | 58.555 | 55.105 | 365 |
| 19 | 2.0000 | 5.000 | 30 | 1.257 | 0.99930 | 6.391 | 1.017 | 1.205 | 61.207 | 57.085 | 349 |
| 20 | 2.1250 | 5.313 | 31.875 | 1.183 | 0.99888 | 6.195 | 0.986 | 1.257 | 63.872 | 59.063 | 367 |
| 21 | 2.2500 | 5.625 | 33.75 | 1.117 | 0.99831 | 6.016 | 0.957 | 1.310 | 66.558 | 61.040 | 353 |
| 22 | 2.3750 | 5.938 | 35.625 | 1.058 | 0.99755 | 5.851 | 0.931 | 1.364 | 69.271 | 63.018 | 362 |
| 23 | 2.5000 | 6.250 | 37.5 | 1.005 | 0.99657 | 5.698 | 0.907 | 1.418 | 72.017 | 65.000 | 347 |
| 24 | 2.6250 | 6.563 | 39.375 | 0.957 | 0.99536 | 5.555 | 0.884 | 1.472 | 74.802 | 66.987 | 369 |
| 25 | 2.7500 | 6.875 | 41.25 | 0.914 | 0.99389 | 5.422 | 0.863 | 1.528 | 77.634 | 68.980 | 351 |
| 26 | 2.8750 | 7.188 | 43.125 | 0.874 | 0.99215 | 5.297 | 0.843 | 1.585 | 80.519 | 70.980 | 364 |
| 27 | 3.0000 | 7.500 | 45 | 0.838 | 0.99012 | 5.179 | 0.824 | 1.643 | 83.464 | 72.990 | 345 |

THIS PAGE INTENTIONALLY LEFT BLANK

# APPENDIX B:
# Linear Superposition Results

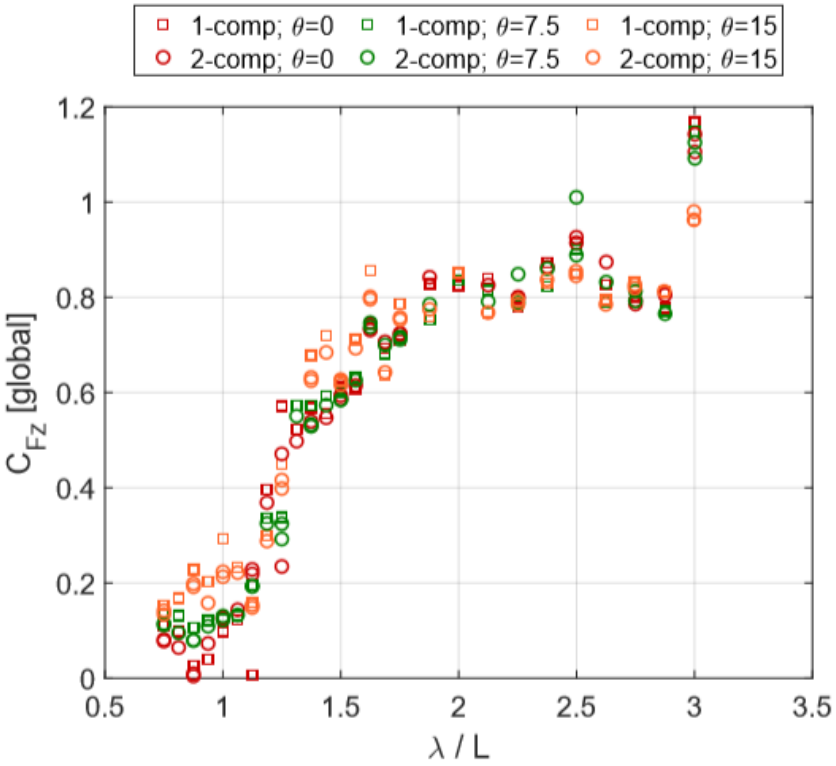


Figure B.1. Linear Superposition—Vertical Force. The non-dimensionalized vertical force in the global coordinate system is shown with non-dimensionalized wavelength. The squares are results from the single, regular wave. The circles are the linear portion of the results from the two-component wave tests. The different colors represent different pitch angles.

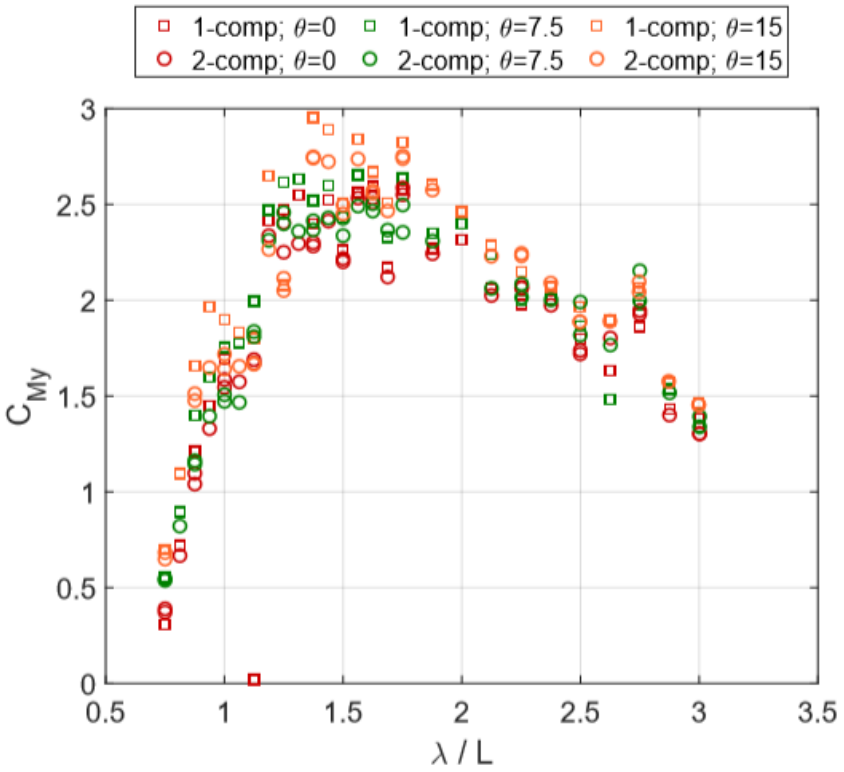


Figure B.2. Linear Superposition—Pitch Moment. The non-dimensionalized pitch moment in the global coordinate system is shown with non-dimensionalized wavelength. The squares are results from the single, regular wave. The circles are the linear portion of the results from the two-component wave tests. The different colors represent different pitch angles.

# APPENDIX C:
# Pitch Effect Results

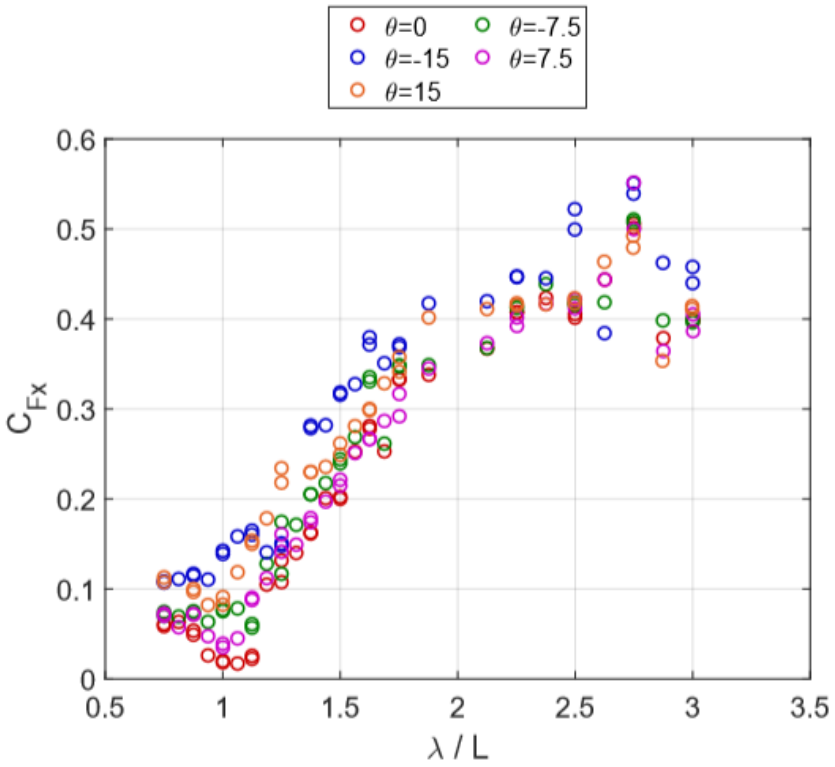


Figure C.1. Pitch Effects—Local Axial Force]. The non-dimensionalized ax-ial force in the local coordinate system is shown with non-dimensionalized wavelength. The different colors represent different pitch angles. Results from single wave and two wave tests are included.

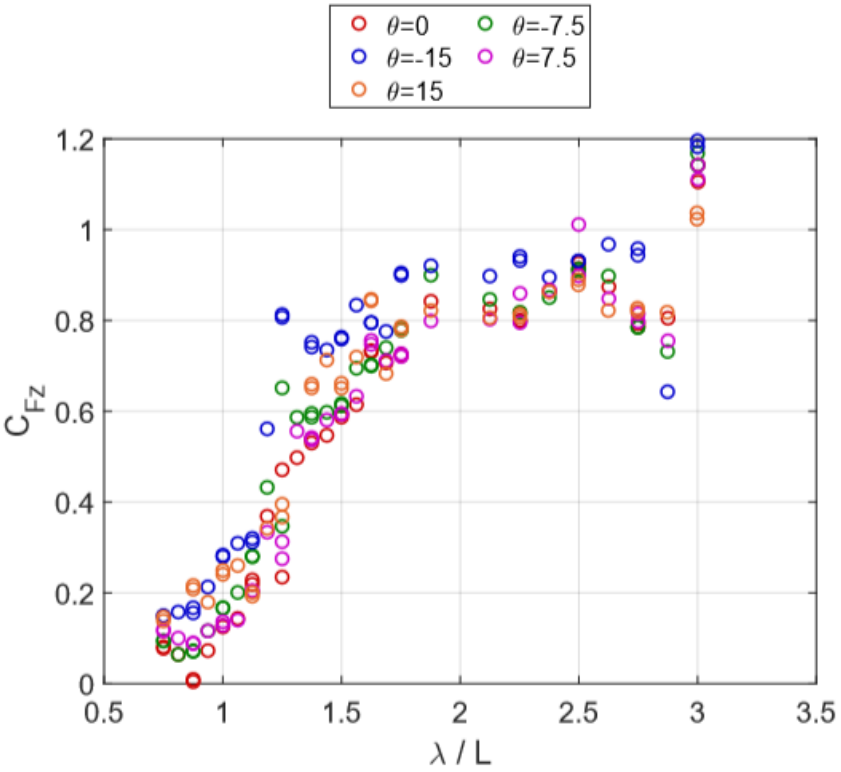


Figure C.2. Pitch Effects—Local Vertical Force. The non-dimensionalized vertical force in the local coordinate system is shown with non-dimensionalized wavelength. The different colors represent different pitch angles. Results from single wave and two wave tests are included.

# List of References


[1] R. O'Rourke, "Navy large unmanned surface and undersea vehicles: Background and issues for Congress," Congressional Research Service, Tech. Rep. R45757, Dec. 2019.

[2] P. Small, "Unmanned maritime systems update," Unmanned Maritime Systems (PMS 406), Tech. Rep., Jan. 2019.

[3] W. Cummins, "Hydrodynamic forces and moments acting on a slender body of revolution moving under a regular train of waves," David W. Taylor Model Basin, Washington D.C., Tech. Rep. 910, Dec. 1954.

[4] C. Lee and J. Newman, "The vertical force and moment of submerged bodies under waves," *Journal of Ship Research*, vol. 15.

[5] P. Wilmott, "On the motion of a slender body submerged beneath surface waves," *Journal of Ship Research*, vol. 32, no. 3.

[6] R. Englert and J. Thune, "Wave forces and moments on a submerged elongated body of revolution," M.S. thesis, Dept. of Naval Architecture and Marine Eng., Massachusetts Institute of Technology, Cambridge, MA, 1961.

[7] J. Pinkster, "Mean and low frequency wave forces on semi-submersibles," in *Proceedings of the 13th Annual Offshore Technology Conference*, Houston, TX, May 1981.

[8] T. Crook, "An initial assessment of free surface effects on submerged bodies," M.S. thesis, Naval Postgraduate School, Monterey, CA, 1994.

[9] P. Ananthakrishnan and K. Zhang, "AUV motion in a wave field," in *OCEANS '98 Conference Proceedings*, Sep. 1998, vol. 2, pp. 1059–1063.

[10] L. Jones, J. Klamo, Y. Kwon, and J. Didoszak, "Numerical and experimental study of wave-induced load effects on a submerged body near the surface," in *Proceedings of the 37th International Conference of Ocean, Offshore, and Arctic Engineering*, Madrid, Spain, June 2018, vol. 7B: Ocean Engineering, p. V07BT06A048; 9 pages.

[11] G. Khalil, "Experimental investigation of wave forces on submerged horizontal cylinders," *Indian Journal of Eng. and Material Sciences*, vol. 8, pp. 59–65, Apr. 2001.

[12] T. M. Turner, "Analyzing uuv hull cross-sections for minimizing wave loads when operating near surface," M.S. thesis, Dept. Systems Eng., Naval Postgraduate School, Monterey, CA, 2018.

[13] K. Suriben, "Study of wave-induced load effects on a submerged body near the surface," M.S. thesis, Dept. Mech. Eng., Naval Postgraduate School, Monterey, CA, 2019.

[14] A. Whitmer, "Predicting wave-induced loads in complex seaways on shallowly submerged vessels," M.S. thesis, Dept. Mech. Eng., Naval Postgraduate School, Monterey, CA, 2018.

[15] T. M. Turner, J. T. Klamo, and Y. W. Kwon, "Comparison of wave-induced loads on a near surface slender body from inviscid flow linear solution and an experimental model test," in *Proceedings of the 37th International Conference on Ocean, Offshore, and Arctic Engineering, Volume 7A*, Madrid, Spain, June 2018.

[16] A. R. Whitmer, J. T. Klamo, and Y. W. Kwon, "On the validity of predicting wave-induced loads on a submerged body using the superposition of regular wave results," in *OCEANS 2019 MTS/IEEE SEATTLE*, Seattle, WA, Jan. 2019, pp. 1–11.

[17] J. Klamo, T. Turner, C. Cool, K. Yeager, and Y. Kwon, "On the accuracy of a theoretical solution for wave-induced loads on an underwater vehicle," Forthcoming.

# Initial Distribution List

1. Defense Technical Information Center
   Ft. Belvoir, Virginia

2. Dudley Knox Library
   Naval Postgraduate School
   Monterey, California